

PIV investigations of shock-buffet dynamics on a supercritical airfoil with a pitching degree of freedom

S. Scharnowski*, T. Baur, A. Accorinti, C. J. Kähler

Institute of Fluid Mechanics and Aerodynamics, Universität der Bundeswehr München, 85577 Neubiberg, Germany

*Corresponding author: sven.scharnowski@unibw.de

Keywords: Transonic Flow, PIV, Flow-structure interaction

ABSTRACT

The interaction between the transonic flow around a spring mounted OAT15A airfoil model and the resulting pitching motion of the model was investigated with the goal of understanding the dynamics of the occurring phenomena. The experiments were performed at free-stream Mach numbers from 0.70 to 0.77 and at a Reynolds number of $Re_c \approx 3 \times 10^6$. The dominant structural frequency of the airfoil's pitch motion was adjusted to be in the range of the natural buffet frequency of the flow with inhibited pitching motion of the model. The variation of the Mach number allowed for an investigation in the pre-buffet, buffet and post-buffet regime. A periodic pitch motion with an amplitude of the angle of attack of up to $\pm 1.17^\circ$ was observed for buffeting flow conditions while it was significantly less in pre-buffet and close to buffet offset conditions. Velocity field measurements by means of high repetition rate particle image velocimetry (PIV) were used to capture the motion of the shock and to determine the state of the boundary layer flow for the different phases of the model motion. For the Mach number range $Ma = 0.72 - 0.75$ the change of the angle of attack and the shock position correlate strongly with each other. From the measurements, the delay of both quantities during the coupled motion could be determined.

1. Introduction

If the transonic flow over an airfoil accelerates to supersonic speed the supersonic region is terminated by means of a compression shock. The pressure rises abruptly and the velocity drops accordingly due to the shock. Depending on the shock strength and the state of the boundary layer, separation can occur due to the sudden increase in pressure. The flow separation affects the flow direction downstream of the shock and causes the shock to move upstream, which affects the separation again. Depending on the airfoil geometry, there is no stable solution for the shock position for a certain range of inflow Mach numbers and angles of attack. In this range the shock executes a periodic motion coupled with a shock-induced separation of the boundary layer, known as shock-buffet (Giannelis et al., 2017; Lee, 2001; McDevitt & Okuno, 1985; Tijdeman, 1977). Shock-induced buffet causes strong periodic pressure fluctuations and limits the operating range

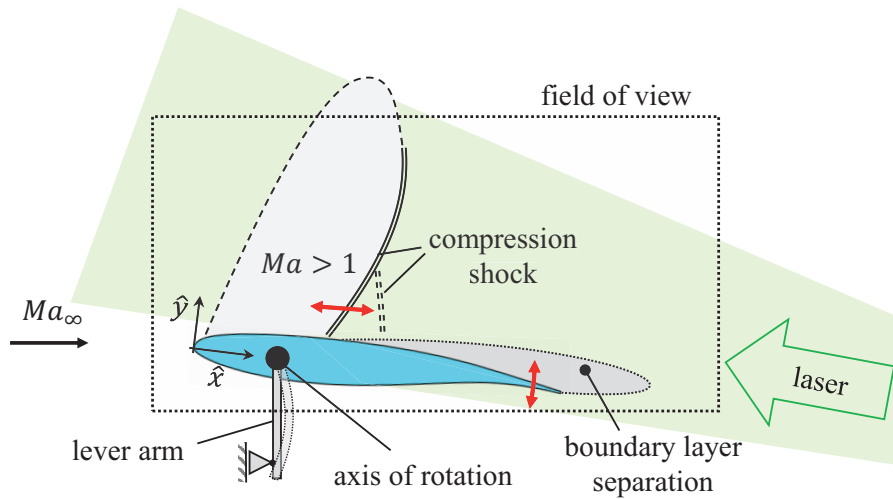


Figure 1. Sketch of the wind tunnel model with the essential flow effects as well as the light sheet and the field of view for the PIV experiments (Scharnowski et al., 2022)

of technical components. The consideration of coupling between fluid and structure is particularly relevant, since real structures are never infinitely stiff. Recent numerical simulations show that the natural frequencies of elastic structures can have an influence on the buffet frequency and on the buffet boundary (Gao & Zhang, 2020; Nitzsche et al., 2019).

In order to analyze the coupling between fluid and structure, a quasi-two-dimensional airfoil model with a pitching degree of freedom whose natural frequency is close to the buffet frequency is investigated in this work. This allows a coupling between the change of the angle of attack and the flow field with oscillating compression shock and changing boundary layer separation.

The following section briefly describes the test facility, the wind tunnel model and the measurement approach. In Sec. 3, the measurement results are presented and discussed in detail, in Sec. 4 the work is summarized and conclusions are drawn.

2. Measurement setup

The measurements were performed in the trisonic wind tunnel at the Bundeswehr University Munich (TWM). The TWM facility is a blow-down type wind tunnel with a 300 mm wide and 675 mm high test section. Two adjustable throats, the Laval nozzle upstream of the test section and the diffuser further downstream, enable an operating range of Mach numbers from 0.2 to 3.0. The facility has two tanks with a total volume of 356 m³ that are pressurized with dry air up to 20 bar above ambient pressure. To control the Reynolds number, the total pressure in the test section is varied between 1.2 and 5 bar. The free-stream turbulence level based on streamwise velocity fluctuations in the TWM test section is approximately 1.3% for the Mach number range considered here. More details about the facility and its characterization are provided in Scheitle & Wagner (1991) and Scharnowski et al. (2019).

Table 1. Summary of the flow conditions for the different wind tunnel runs together with statistical results of the airfoil dynamics and the shock dynamics. The dimensionless frequency of the shock motion is computed using $k = \pi f_{\hat{x}_s} c / u_\infty$ and τ_0 is the phase difference between shock motion and angle of attack.

Ma	Re_c	$\bar{\alpha} \pm \Delta\alpha$	f_α	$f_{\hat{x}_s}$	k	τ_0
0.70	$2.96 \cdot 10^6$	$6.04^\circ \pm 0.28^\circ$	108.6 Hz	–	–	–
0.72	$3.01 \cdot 10^6$	$5.91^\circ \pm 0.96^\circ$	113.3 Hz	113.3 Hz	0.229	1.02 ms
0.74	$3.06 \cdot 10^6$	$5.76^\circ \pm 1.17^\circ$	115.4 Hz	115.5 Hz	0.228	1.47 ms
0.75	$3.05 \cdot 10^6$	$5.70^\circ \pm 1.17^\circ$	116.8 Hz	116.8 Hz	0.227	1.57 ms
0.77	$3.11 \cdot 10^6$	$5.64^\circ \pm 0.45^\circ$	118.2 Hz	123.8 Hz	0.235	–

The airfoil model consists of a shell-like structure (carbon-fiber reinforced plastic, CFRP) and a metal shaft (tool steel, Toolox44) located at 25 % of the chord length. The shaft passes through the side windows of the test section and is supported by needle bearings directly outside the windows. With this support, the model can rotate around the axis of the shaft, as illustrated in Fig. 1. A steel lever with a rectangular cross-section ($6 \times 10 \text{ mm}^2$) extends downwards from both shaft ends. This lever serves as a spring and its bending stiffness can be adjusted via the lever length. Balancing masses are used to ensure that the center of gravity of all moving parts is located on the axis of rotation. Thus, structural pitch and heave modes are decoupled in wind-off conditions. The natural frequency of the model's pitch motion was set to 105 Hz, which is approximately the same as the buffet frequency of the rigidly suspended airfoil, according to Kokmanian et al. (2022).

For the geometry, the super-critical shape OAT15A was chosen. The model has a chord length of 150 mm and is 298 mm wide. This results in a gap of one millimeter on each side, which is required to perform the pitch motion.

The Mach number of the flow was varied between $Ma = 0.70$ and 0.77 , where the static pressure port from which Ma is computed is located 200 mm upstream of the model at the upper wall of the test section. A total pressure of $p_0 = 1.5 \text{ bar}$ was used to achieve a Reynolds number of $Re_c \approx 3.0 \times 10^6$. This value is based on the chord length $c = 150 \text{ mm}$. Values for the flow conditions of the different wind tunnel runs are summarized in Table 1.

For the PIV measurements, the flow was seeded with Di-Ethyl-Hexyl-Sebacat (DEHS) tracer particles with a mean diameter below 1 μm . The particles have a response time of about 2 s (Melling, 1997; Ragni et al., 2011) and are therefore considered to be able to follow the flow sufficiently.

The particles in the TWM test section were illuminated from downstream with a light sheet generated by a PIV double pulse laser (DM 150-532, by Photonics Industries Inc.) with a light sheet width of 0.5 mm measured at $1/e^2$ of the maximum intensity. The scattered light was recorded by means of a high speed camera (Phantom V2640, by Vision Research Inc.) which was equipped with a 50 mm lens (Planar T2/50, by Zeiss). For statistical convergence of the results, 10,000 double images, 2048×1264 pixel in size (corresponding to $278 \times 171 \text{ mm}^2$), were recorded with 5 kHz. The time separation between the double images was set to 4 s, resulting in a particle image displace-

ment of up to 12 pixel for regions with a flow velocity of 400 m/s.

Although the optical magnification and the particle image displacement were optimized to account for the richness of spatial and temporal dynamics in this kind of flow, resolving the small-scale features remains challenging due to the strong velocity gradients in the shear layers (Scharnowski & Kähler, 2020). For the densely seeded PIV images, a background noise level with a standard deviation of about 12 counts was estimated from the auto-correlation function with the method presented in Scharnowski & Kähler (2016). This noise level leads to a loss-of-correlation due to image noise of $F_\sigma \approx 0.9$ and to a signal-to-noise ratio of $\text{SNR} \approx 3.6$, which is considered to be well suited for PIV evaluation.

3. Results and Discussions

3.1. Structural dynamics

Before the wind tunnel run, the angle of attack α was set to 7.0° with an unloaded lever arm. During the wind tunnel run, the aerodynamic loads caused a positive aerodynamic moment that bent the lever arm and decreased α on average to a value between $\bar{\alpha} = 5.64^\circ$ and 6.04° , depending on the free-stream Mach number (see Tab. 1). Additionally, the angle of attack is fluctuating around its mean with an amplitude of up to $\Delta\alpha = \pm 1.17^\circ$ for a Mach number of 0.74 and 0.75. For the highest and the lowest Mach numbers however, the fluctuation amplitude is significantly smaller.

The pitching motion is highly periodic, as can be seen from the power spectral density on the left side of Fig. 2. The dominant frequency is slightly larger than the natural frequency of the model's pitch motion (105 Hz) and increases with larger Mach number.

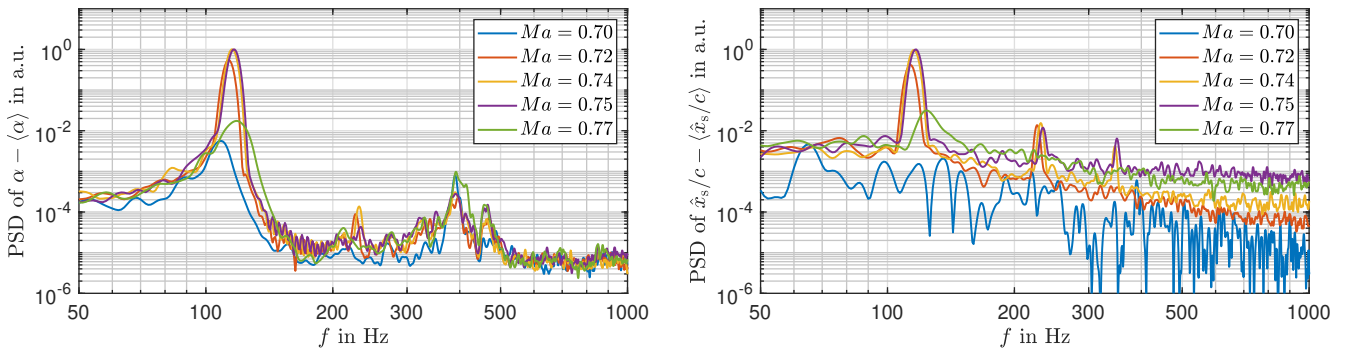


Figure 2. Power spectral density of the angle of attack α (*left*) and the shock-foot location \hat{x}_s (*right*) for the investigated Mach numbers.

3.2. Shock dynamics

The change of the angle of attack is related to the shock oscillation in the flow field which is accompanied by a change of the state of the boundary layer flow. To determine reliable velocity fields,

the PIV images were evaluated using an iterative approach with decreasing interrogation window size and subsequent image deformation. A Gaussian window weighting function was applied and a final interrogation window size of 24^2 pixel with 50% overlap was used, leading to a vector grid spacing of 1.6 mm corresponding to 1.1% of the chord length c . Invalid vectors were identified and removed with the method of Westerweel & Scarano (2005). For most time steps, the fraction of invalid vectors was well below 1%.

Figure 3 shows example velocity field for the different Mach numbers. For each case, examples of the extreme shock positions are shown. The shock was identified from the strongest gradient $\partial u/\partial x$ and is shown as a solid line in the figure. A second order polynomial fit function was applied to the lower part of the detected shock and extrapolated to the airfoil's surface in order to obtain the shock's foot location.

The shock dynamics strongly depend on the Mach number case, as can be seen in Fig. 3 as well as from the spectra in Fig. 2 on the right side. For $Ma = 0.70$ the shock oscillation is rather limited. Furthermore, the boundary layer seems to be fully attached during all phases of the shock motion. With increasing Mach number, shock buffet occurs, which is characterized by an alternating attached and detached boundary layer flow combined with a strong shock oscillation, as can be seen in the second and third row in Fig. 3. When reaching $Ma = 0.77$, the shock oscillation reduces again. Under these flow conditions, the boundary layer is permanently detached regardless of where the compression shock is located. One way to determine the state of the boundary layer is to find the shock angle β . Where β is the angle between the model surface and the shock at the shock foot. Figure 4 shows a histogram of β for the different test cases. Theoretically, β can take values between the Mach angle of the local Mach number and 90° . The larger the shock angle, the stronger the shock and thus the pressure rise across it. However, if a strong shock leads to a separation, the flow direction and thus also the shock angle change again, causing the shock to weaken. In the buffet case, the shock angle changes periodically causing the bimodal distribution of β for $Ma = 0.72 - 0.75$ in Fig. 4. Outside the buffet boundaries, the boundary layer flow is either always attached or always detached causing a narrower distribution function with a maximum at approximately $\beta = 75^\circ$ for $Ma = 0.70$ and $\beta = 50^\circ$ for $Ma = 0.77$.

3.3. Fluid structure coupling

If the buffet frequency is close to the pitching frequency, a synchronized motion of the shock and the airfoil is possible. Figure 5 shows the shock-foot location and the angle of attack for 200 successive time steps in the top left. It is clear from the figure that for $Ma = 0.72 - 0.75$, both quantities are directly coupled. The shape of the function for $\alpha(\hat{x}_s)$ corresponds approximately to an ellipse, which results from a phase difference of the two quantities. In contrast, for the pre-buffet and the post-buffet cases, shock location and angle of attack seem to be independent.

The correlation coefficient and the phase difference was evaluated from the following correlation

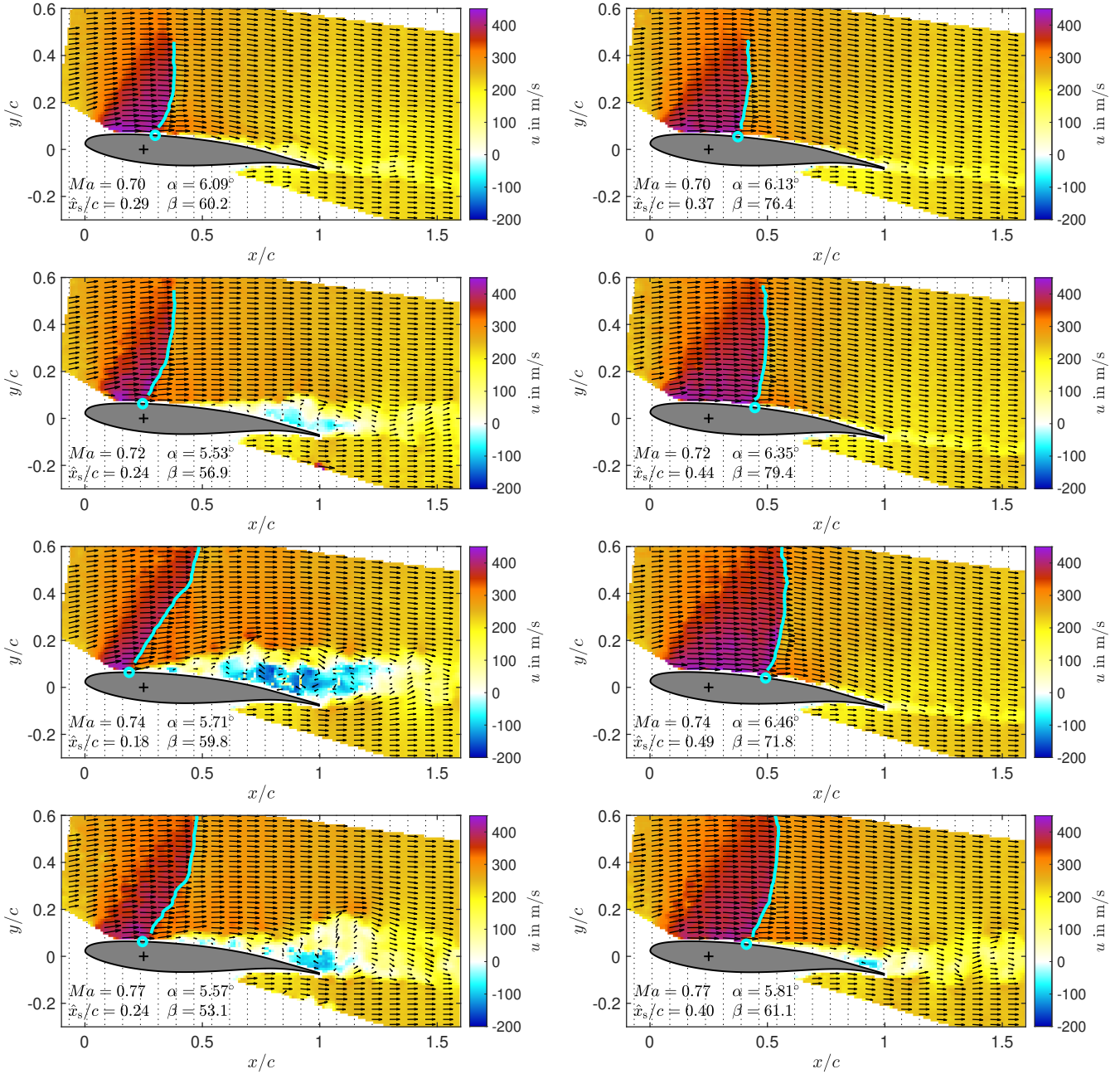


Figure 3. Examples flow fields with the shock located at an extreme upstream (*left*) and an extreme downstream (*right*) location for Mach numbers between $Ma = 0.70$ and 0.77 (from *top* to *bottom*). The solid lines indicate the detected shock position and the open circles show the extrapolated shock-foot location on the airfoil's surface.

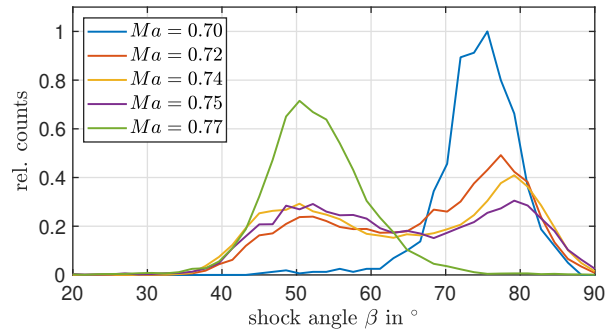


Figure 4. Shock-foot location and angle of attack for different free-stream Mach numbers. Top left: Development of α and x_s over 200 successive time steps. Bottom: Shock-foot location probability distribution. Right: Angle-of-attack probability distribution.

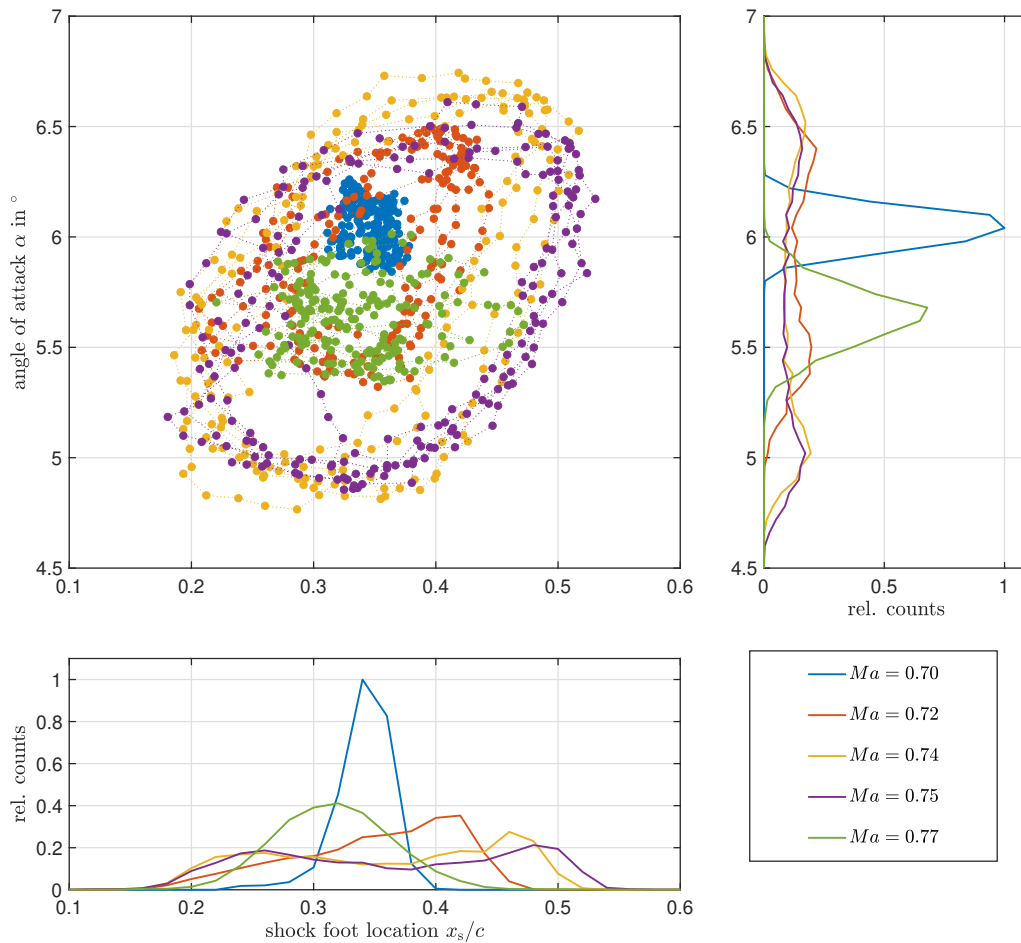


Figure 5. Shock-foot location and angle of attack for different free-stream Mach numbers. Top left: Development of α and x_s over 200 successive time steps. Bottom: Shock-foot location probability distribution. Right: Angle-of-attack probability distribution.

function:

$$R_{\alpha, \hat{x}_s}(\tau) = \frac{\sum_{n=1}^N \alpha'(t - \tau) \cdot \hat{x}_s'(t)}{N \cdot \sigma_\alpha \cdot \sigma_{\hat{x}_s}} \quad (1)$$

Where α' , \hat{x}_s' and σ_α , $\sigma_{\hat{x}_s}$ are the fluctuation values about the mean and the standard deviation, respectively. The time shift τ is used to analyze the temporal evolution of the correlation function.

The correlation value is shown in Fig. 6 as a function of τ for the different Mach numbers. The figure shows very good correlation for $Ma = 0.72 - 0.75$ with a delay between $\tau = 1.02$ ms and 1.57 ms, as summarized in Tab. 1. The pre-buffet and the post-buffet cases show a weak correlation as expected from the development of α and x_s in Fig. 5.

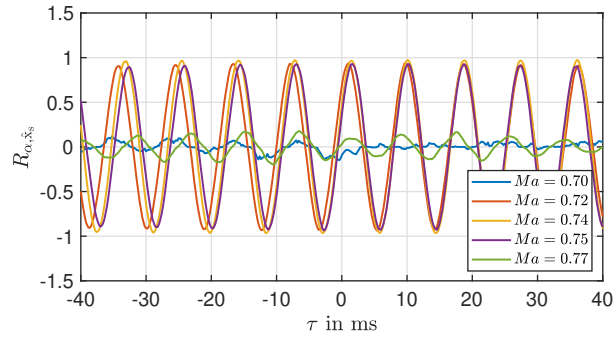


Figure 6. Correlation of angle of attack α and shock-foot location \hat{x}_s as a function of the delay time τ according to Eq. (1)

4. Summary and conclusions

The transonic flow over an OAT15A airfoil model with a torsional degree of freedom was investigated by means of high repetition rate PIV measurements. At buffet flow conditions, a coupled periodic change of the angle of attack and the shock position was observed. A correlation of both quantities showed a delay of 12% to 18% of the period time, where the angle of attack reaches its maximum later than the shock position.

It was shown that during the buffet cycle, the flow strongly varies regarding the shape and location of the compression shock as well as the state of the boundary layer downstream of the shock. For the investigated test cases, the rotational degree of freedom significantly enhances the dynamics of the flow field compared to a model with zero degree of freedom (Kokmanian et al., 2022).

Acknowledgements

Financial support in the frame of the project HOMER (Holistic Optical Metrology for Aero-Elastic Research) from the European Union's Horizon 2020 research and innovation program under grant agreement No. 769237 is gratefully acknowledged. Furthermore, the authors would like to thank

Jens Nitzsche, Yves Govers, Johannes Dillinger, Johannes Knebusch and Tobias Meier for their contributions during the model design phase of the project.

References

- Gao, C., & Zhang, W. (2020). Transonic aeroelasticity: A new perspective from the fluid mode. *Progress in Aerospace Sciences*, 113, 100596. Retrieved from <https://doi.org/10.1016/j.paerosci.2019.100596>
- Giannelis, N. F., Vio, G. A., & Levinski, O. (2017). A review of recent developments in the understanding of transonic shock buffet. *Progress in Aerospace Sciences*, 92, 39-84. Retrieved from <https://doi.org/10.1016/j.paerosci.2017.05.004>
- Kokmanian, K., Scharnowski, S., Schäfer, C., Accorinti, A., Baur, T., & Kähler, C. J. (2022). Effect of Mach Number and Angle of Attack on Transonic Shock Buffet over a Supercritical Airfoil using Particle Image Velocimetry. *Experiments in Fluids*, under review.
- Lee, B. H. K. (2001). Self-sustained shock oscillations on airfoils at transonic speeds. *Progress in Aerospace Sciences*, 37(2), 147–196. Retrieved from [https://doi.org/10.1016/S0376-0421\(01\)00003-3](https://doi.org/10.1016/S0376-0421(01)00003-3)
- McDevitt, J. B., & Okuno, A. F. (1985). *Static and dynamic pressure measurements on a NACA 0012 airfoil in the Ames high Reynolds number facility* (Vol. 2485; Tech. Rep.).
- Melling, A. (1997). Tracer particles and seeding for particle image velocimetry. *Meas Sci Tech*, 8, 1406-1416. Retrieved from <http://dx.doi.org/10.1088/0957-0233/8/12/005>
- Nitzsche, J., Ringel, L. M., Kaiser, C., & Hennings, H. (2019, June). Fluid-mode flutter in plane transonic flows. In *Ifasd 2019 international forum on aeroelasticity and structural dynamics*. Retrieved from <https://elib.dlr.de/127989/>
- Ragni, D., Schrijer, F., Van Oudheusden, B. W., & Scarano, F. (2011). Particle tracer response across shocks measured by PIV. *Experiments in Fluids*, 50(1), 53–64. Retrieved from <http://dx.doi.org/10.1007/s00348-010-0892-2>
- Scharnowski, S., Bross, M., & Kähler, C. J. (2019). Accurate turbulence level estimations using PIV/PTV. *Experiments in Fluids*, 60(1), 1. Retrieved from <https://doi.org/10.1007/s00348-018-2646-5>
- Scharnowski, S., & Kähler, C. J. (2016). On the loss-of-correlation due to PIV image noise. *Experiments in Fluids*, 57(7), 1–12. Retrieved from <http://dx.doi.org/10.1007/s00348-016-2203-z> doi: 10.1007/s00348-016-2203-z

- Scharnowski, S., & Kähler, C. J. (2020). Particle Image Velocimetry – classical operating rules from today's perspective. *Optics and Lasers in Engineering*, 106185. Retrieved from <https://doi.org/10.1016/j.optlaseng.2020.106185>
- Scharnowski, S., Kokmanian, K., Schäfer, C., Baur, T., Accorinti, A., & Kähler, C. J. (2022). Shock-buffet analysis on a supercritical airfoil with a pitching degree of freedom. *Experiments in Fluids*, 63(6), 93. Retrieved from <https://doi.org/10.1007/s00348-022-03427-4>
- Scheitle, H., & Wagner, S. (1991). Influences of wind tunnel parameters on airfoil characteristics at high subsonic speeds. *Experiments in Fluids*, 12(1-2), 90–96. Retrieved from <https://doi.org/10.1007/BF00226571>
- Tijdeman, H. (1977). Investigations of the transonic flow around oscillating airfoils. *NLR-TR 77090 U*.
- Westerweel, J., & Scarano, F. (2005). Universal outlier detection for PIV data. *Experiments in Fluids*, 39, 1096-1100. Retrieved from <http://dx.doi.org/10.1007/s00348-005-0016-6>